Advances in Science and Technology Research Journal

Advances in Science and Technology Research Journal, 2025, 19(5), 422–429
https://doi.org/10.12913/22998624/202696
ISSN 2299-8624, License CC-BY 4.0

Received: 2025.01.18
Accepted: 2025.03.15
Published: 2025.04.01

Ductile iron crossbeam integrated parts casting process and shrinkage analysis

Li Heng[1,2*], Guo Wang[1,2], Zhao Yongzheng[3], Zhang Weiguang[3], Wu Yucheng[1,2]

[1] School of materials science and engineering, Hefei University of Technology, Hefei 230009, China
[2] Anhui Province Key Lab of Aerospace Structural Parts Forming Technology and Equipment, Hefei University of Technology, Hefei 230009, China
[3] Hefei Jianghuai Casting Co., LTD., Hefei 230009, China
* Corresponding author's e-mail: liheng0205@hfut.edu.cn

ABSTRACT

A composite component has been developed to replace the conventional multi-part crossbeam assembly, with its sand casting technique optimized for truck chassis. Computational modeling and experimental methods are employed to simulate the sand casting process, focusing on filling, solidification, temperature distribution, liquid phase dispersion, and shrinkage. The study also fine-tunes the quantity and placement of risers. To minimize defects, the casting parameters are set as follows: pouring temperature of 1380 °C, pouring speed of 10 cm/s, and mold preheating temperature of 20 °C. This optimized process resulted in a 9.36% reduction in shrinkage compared to the original design. Experimental results indicate that the castings exhibit a spheroidization grade of 2, pearlite content ≥ 90%, tensile strength ≥ 854 MPa, elongation ≥ 6%, and are free from cracks and shrinkage in the critical load-bearing sections, thus meeting the required application standards.

Keywords: ductile iron, crossbeam, structural integration, process optimization, numerical simulation.

INTRODUCTION

The load-bearing performance of truck crossbeams is critical to vehicle safety [1]. As a structural component, the design of the crossbeam prioritizes safety, which historically has led to the use of multi-part assemblies. However, this approach results in a complex manufacturing process that is increasingly at odds with modern cost reduction objectives, efficiency, and environmental sustainability.

With the growing emphasis on automobile lightweighting, research into lighter automotive structures has deepened in recent years [2, 3]. Much attention has been paid to the optimal design of beam structure, Wang et al. found that when optimizing a thin-walled beam structure, the monolithic update scheme typically navigates a larger design space than the two staggered update schemes, for most cases examined it provides the lowest structural compliance. [4] Weeger et al. proposed an isogeometric optimization method for nonlinear 3D beams and verified its universality [5]. In terms of manufacturing processes, ductile iron—a material with mechanical properties comparable to steel and a simpler production process—is frequently used in the construction of truck crossbeams [6]. However, the complexity of its solidification process poses challenges in relying solely on empirical methods for process design, making numerical simulations a common tool to predict defects in ductile iron components [7, 8]. At present, the process design of ductile iron castings normally uses a combination of calculation and experimental methods [9, 10]. Jinhai Liu et al. investigated the precipitation and evolution of graphite spheres in sub-eutectic, eutectic, and peritectic ductile irons and concluded that eutectic ductile irons have the least tendency to shrink [11]. Deng Yizhao utilized ProCAST simulation software to analyze various process options, optimize riser and cold iron settings, and effectively reduce casting shrinkage [12]. Xiang Siyu, using ProCAST, numerically

simulated the casting process for two different gating systems—ladder and top injection. The study concluded that top injection was more effective in compensating for shrinkage, while the ladder system was better for filling. [13]

Despite these advances, research on structural integration and process optimization remains scarce in truck manufacturing. This study focuses on the integrated ductile iron truck crossbeam, using Flow-3D software to analyze the filling, solidification temperature field, solid-phase dispersion, and defect formation [14]. By optimizing the casting process, the study contributes to reducing weight, improving casting efficiency, and advancing the lightweight design of heavy-duty trucks.

STRUCTURE AND METHODS

Integrated crossbeam design

The original crossbeam of the heavy truck weighs 50.5 kg and consists of seven parts: four L-shaped steel components, two fixing seats, and one U-shaped steel component, each made from different materials. The main technical parameters of the beam are summarized in Table 1. Based on the technical drawing and the actual structural parameters, a solid model of the beam is created, as shown in Figure 1(a).

Figure 1(a) illustrates the complex design of the beam structure, which requires the machining, assembly, and shaping of seven separate components, each with a detailed manufacturing process. In this study, the crossbeam structure is optimized to achieve a lightweight design.

Figure 1(b) presents a refined 3D model of the crossbeam, with dimensions of 839 × 403 × 221 mm, and a theoretical mass of 36 kg. The chosen casting material is 800-5 ductile iron. The average wall thickness of the crossbeam is 15.96 mm, with area A having the thinnest wall at 8.0 mm and area B having the thickest at 55.5 mm, indicating a significant variation in wall thickness.

Casting process program

In line with the structural characteristics of the crossbeam and the principles of casting process design, a 3D model of the gating system is developed, as shown in Figure 1(b). A closed gating system is selected, with four ingates designed to promote fast and uniform filling of the mold. Each gate is trapezoidal in shape, which can solidify in time after pouring and prevent the liquid iron from flowing back into the cavity.

The ratio of cross-sectional areas in the gating system is designed as follows: F_{sprue}: F_{runner}: F_{ingate} = 2.50: 1.25: 1. This configuration results in the ingate having a cross-sectional area of 1200 mm², the runner 1500 mm², and the sprue 3000 mm², ensuring a smooth and sufficient flow of liquid iron during the casting process.

Figure 2 shows the discretization model. The 3D model of the crossbeam and the gating system is discretized using a mesh size of 2 mm with a grid type of Meshing, yielding a

Table 1. The main technical parameters of the beam

Character radical	Makings	Modulus of elasticity (MPa)	Yield strength (MPa)	Poisson's ratio	Mass (kg)	Overall size (mm)
Mounts	qT550	172000	320	0.275	9.78 × 2	814 × 237 × 600
Steel plate	b510L	200000	355	0.3	(4.46 + 5.07) × 2	

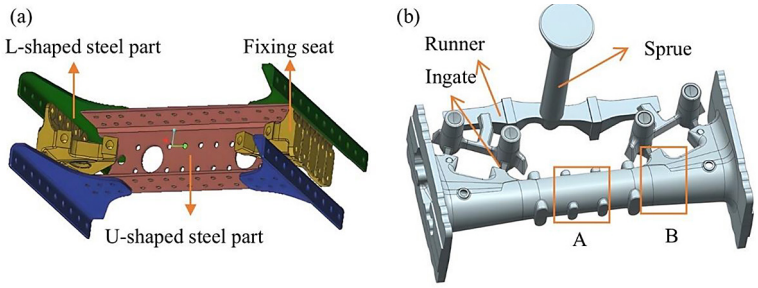

Figure 1. (a) 3D model of the original crossbeam structure;(b) 3D model of the integrated crossbeam and gating system

total of 1.79×10^7 elements. The boundary conditions and initial settings are: the casting material is ductile iron 800-5, sand molds and cores made of furan resin sand. Table 2 presents the parameter values specifically at 1145 °C. The heat transfer coefficient at the interface between the casting and the mold is set to 700 W/(m²·K), with a pouring temperature of 1380 °C and a pouring speed of 10 cm/s. The gravity direction is aligned with the negative normal direction of the sprue plane, with a value of 980 cm/s². The initial temperature of the casting is set to room temperature (25 °C).

RESULTS AND DISCUSSION

Analysis of simulation results

The filling simulation process is presented with pouring temperature as a reference. The temperature distribution during the filling process is analyzed based on the liquid metal flow rate at several key time points: 1.06 s, 3.31 s, 5.04 s, and 8.00 s (corresponding to 5%, 25%, 50%, and 99% filling, respectively), as shown in Figure 3.

- At 1.06 s, the liquid iron flows from the straight channel into the cross channel and fills the entire cross channel rapidly.
- At 3.31 s, the liquid metal splits into four fine streams through the cross-cast channels and spreads evenly over the bottom of the cavity.
- At 5.04 s, the liquid metal flows smoothly in the cavity, creating a uniform liquid surface without turbulence or air entrapment.
- By 8.00 s, the casting reaches 99% of its fill, completing the process without cold segregation or underpouring.

These observations confirm that the closed gating system facilitates a smooth and large flow of liquid iron, ensuring uniform filling and consistent quality of the casting across all positions.

Figure 4 illustrates the right side of the casting, with Figure 4(a) showing the solidification times for different regions of the casting. During the solidification process, thin-walled areas solidify first, while the thick-walled sections at the ends of the casting require the longest solidification time and cannot be supplemented with liquid metal. In these regions, only graphitized expansion can compensate for the contraction of the liquid metal during solidification, which can easily lead to the formation of a molten pool.Figure 4(b) presents the distribution of the liquid phase just prior to complete solidification (99% solidification). It shows the presence of isolated liquid-phase zones in the thick-walled

Table 2. Physical parameters of 800-5

Density (kg·m^{-3})	Liquidus/solidus (K)	Latent heat (kJ·kg^{-1})	Specific heat (kJ·kg^{-1}K^{-1})
6459	1418/1417	210	0.78

Note: at 1145 °C.

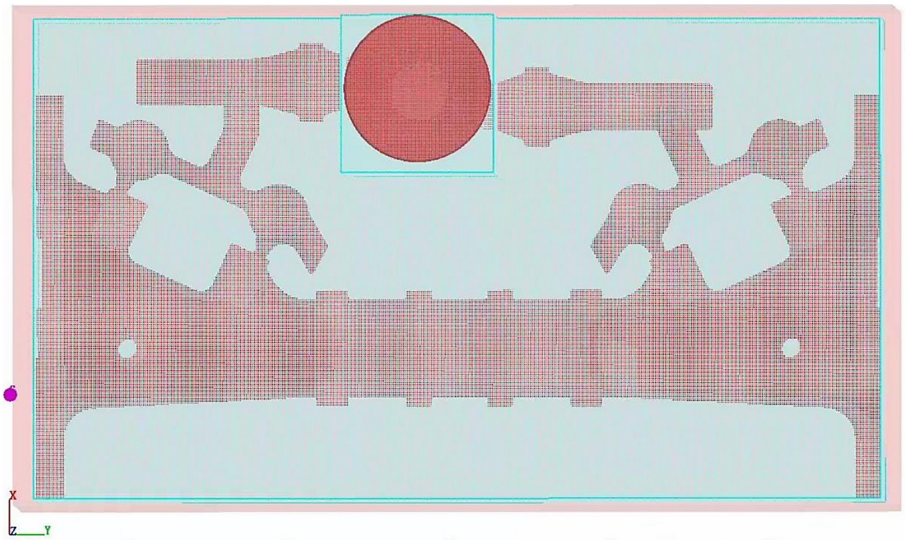

Figure 2. Discretization model of crossbeam

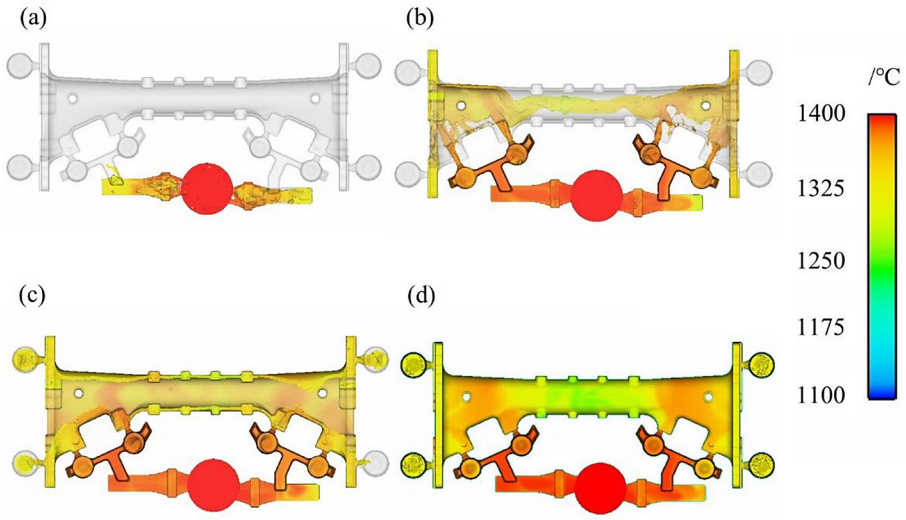

Figure 3. Transverse crossbeam filling process: (a) t = 1.06 s; (b) t = 3.31 s; (c) t = 5.04 s; (d) t = 8.00 s

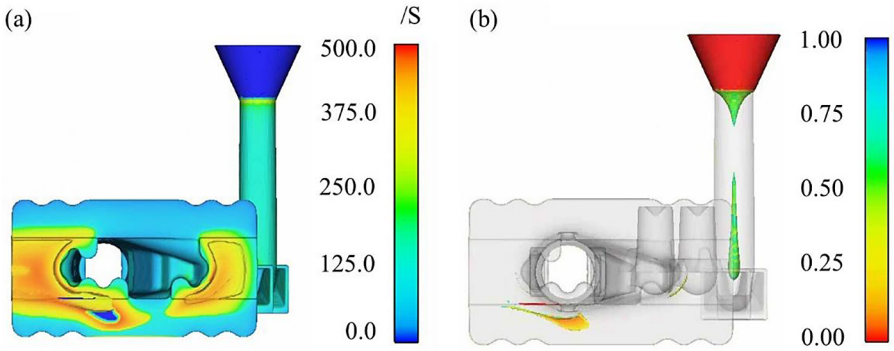

Figure 4. Solidification process: (a) Solidification time; (b) Liquid phase distribution before complete solidification

regions, which are characterized by complex shapes and slow liquid metal flow. These areas become the final solidification zones, hindering the contraction compensation effect in the liquid-phase regions. When these isolated zones cannot be fully filled with liquid metal, shrinkage defects form, leading to shrinkage or incomplete solidification.

In combination, Figure 4(a) and Figure 4(b) reveal that there is a lack of complementary shrinkage at both ends of the casting during solidification, which results in partial collapse zones. These issues prevent the casting from meeting the required specifications, as the liquid phase is unable to fully fill the casting at these locations, leading to shrinkage and potential defects.

Optimization options and analysis

In order to make up the shrinkage of the castings during solidification, eliminate the solidification collapse zone, and reduce the shrinkage and shrinkage defects, the number and distribution of the risers are optimized by improving the problems of the initial scheme. The number and distribution of risers are optimized by adding risers ($4 \times \phi 70 \times 120$ mm) at both ends of the crossbeam to enhance the shrinkage capacity during solidification and reduce the solidification defects of the castings.

Numerical simulation of the optimized casting model is carried out without changing the casting process conditions, and the solidification simulation results of the castings are shown in Figure 5. In Figure 5(a) the solidification time graph of the casting can be seen that the solidification time at both ends of the casting is significantly reduced from 376 s to 127 s compared with the original process scheme. At the same time, the risers at both ends provide the flowing metal liquid during the solidification process, which eliminates the isolated molten pool region under the original process. Figure 5(b) shows the liquid phase distribution of

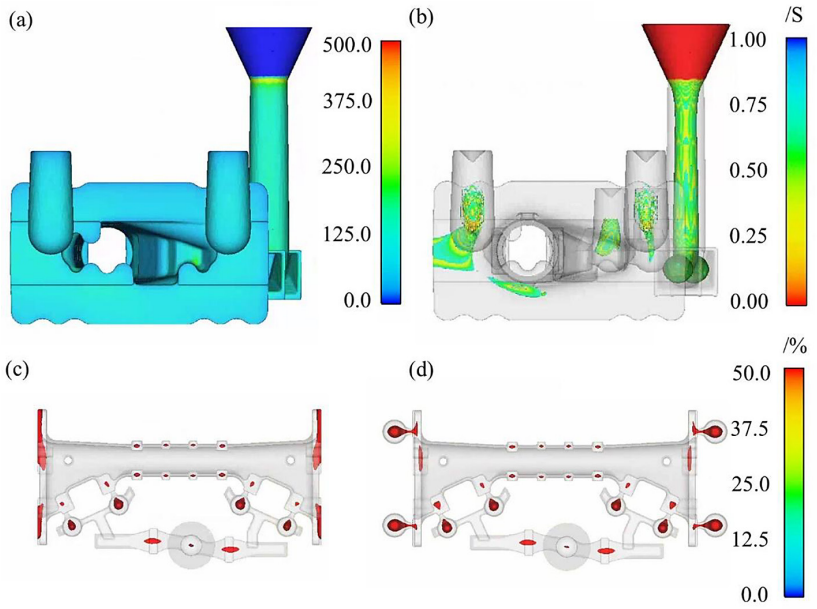

Figure 5. Solidification process of the casting for the optimized solution: (a)solidification time; (b) liquid phase distribution before complete solidification; Distribution of shrinkage in the casting: (c) initial solution; (d) optimized solution

the casting before complete solidification, and it can be seen that the final solidification region in the improved process scheme is mainly located in the part of the gating system. Figure 5(c) and Figure 5(d) display the distribution of shrinkage for the initial and optimized gating systems, respectively. Figure 5(c) highlights the presence of obvious collapse zones at both ends of the casting in the original system, whereas Figure 5(d) shows that the collapse at both ends has been eliminated in the optimized process. The location of shrinkage correlates with the liquid phase areas shown in Figure 5(b), indicating that shrinkage occurs in regions where the liquid phase is isolated during solidification. Software analysis of shrinkage volumes after solidification in both gating systems reveals that the volume of shrinkage in the initial design is 751.16 mm³, while in the optimized design it is reduced to 680.85 mm³, a 9.36% reduction. Additionally, compared to the initial design, the distribution of shrinkage in the optimized system is more uniform and localized in regions where mechanical properties are less critical. Most of the defects are concentrated in the riser areas, which help collect gas and oxidation slag, ultimately improving the casting's overall performance.

Experimental validation

Scrap steel, pig iron, ferromanganese, and intermediate alloys (such as ferromolybdenum) were used as raw materials for melting. The raw materials were melted and discharged from the furnace at temperatures between 1490 °C and 1520 °C. The core wire feeding method was employed to introduce 1.4% FeSiMg6RE2 for spheroidization, and 0.5% and 0.3% Si-Ba were added through in-package gestation and in-flow gestation methods, respectively. The casting process was carried out at 1385 °C to 1410 °C after slag removal, yielding tensile specimens and crossbeam castings.

To verify the effectiveness of the optimized process, samples were taken from different locations on the casting (1: central, 2: near gate, 3: far gate), as shown in Figure 6, for metallographic and organizational property analysis.

Figure 7 presents the graphite morphology and metallographic structure of the specimens from different crossbeam locations. Figure 7(a), (c), and (e) correspond to specimens 1, 2, and 3, respectively. The spheroidization grade and graphite ball size are determined according to the GB/T 9441-2021 standard for "Metallographic examination of ductile iron". The results show that all specimens exhibit a spheroidization grade of 2, with graphite ball sizes ranging from grades 6 to 7 (Table 3).

- Specimen 1 (near-gate region, Figure 7(a)) has the largest average graphite ball size and the smallest number of graphite balls (180 balls/mm²) due to its slow cooling rate.

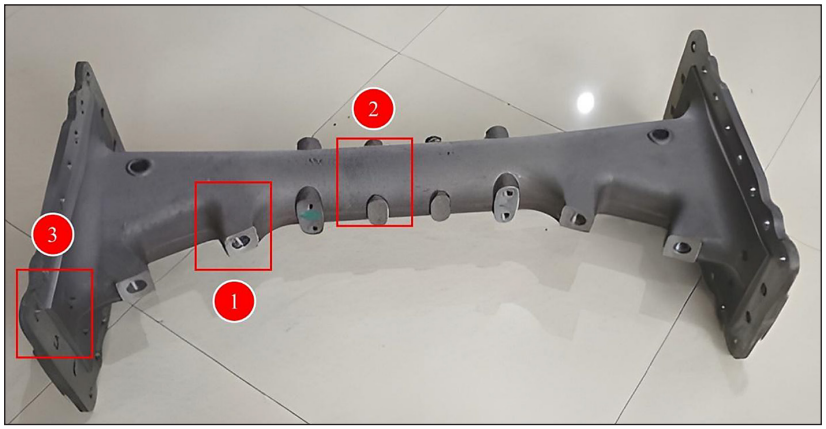

Figure 6. Crossbeam sampling location

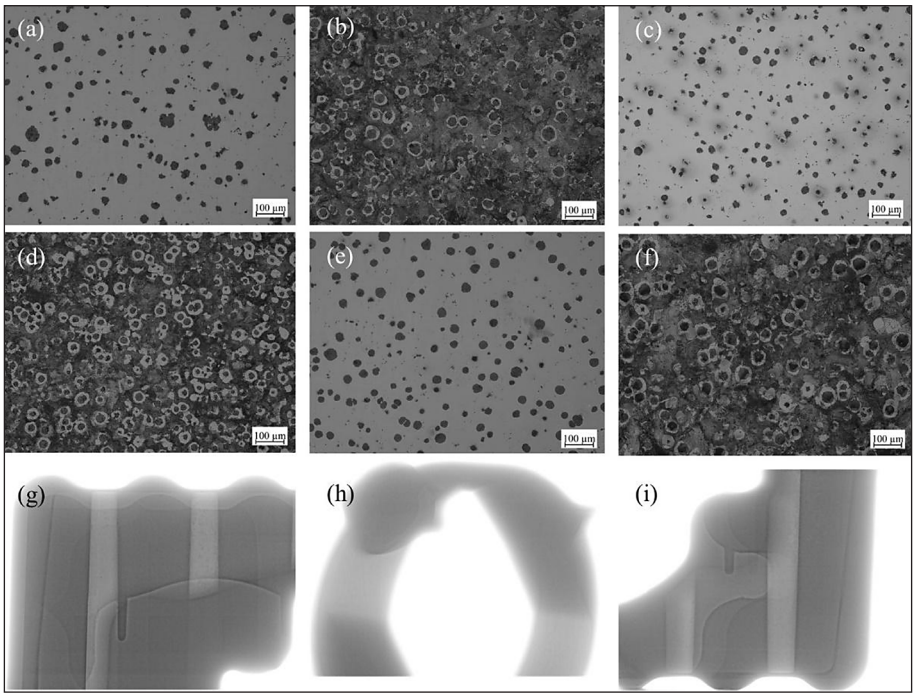

Figure 7. Graphite morphology and metallurgical organization of cast ductile iron; X-ray flaw detection diagrams

Table 3. Metallurgical grading results for each sample

Serial number	Spheroidization grade (level)	Graphite size (grade)	Pearlitic content (%)	Carbide (%)	Phosphorus eutectic (%)
1	2	6	≧90	1	-
2	2	6	≧90	1	-
3	2	7	≧95	1	-

- Specimen 2 (middle region, thin-walled, Figure 7(c)) has the smallest average graphite ball size and the highest number of graphite balls (252 balls/mm²) due to the fastest cooling rate.
- Specimen 3 (far-gate region, Figure 7(e)) has uniform graphite size and an intermediate number of graphite balls (212 balls/mm²).

Figure 7(b), (d), and (f) show the metallographic structures of the specimens, revealing a microstructure composed of black spheroidal graphite, white ferrite, and grey-black pearlite, with over 90% pearlite content. Figure 7(g) and (i) display X-ray inspections of the far-gate area, while Figure 7(h) shows the X-ray inspection of

Table 4. Tensile properties of cast crossbeams

Serial number	Yield strength ($R_{p0.2}$/MPa)	Tensile strength (R_m/MPa)	Elongation (A%)
A	546	875	7.6
B	562	891	6.0
C	552	854	6.5

Table 5. Hardness test table for different positions of the crossbeam

Serial number	Hardness (HV)			Average value (HV)
	1	2	3	
1	280.8	285.8	285.8	284.1
2	272.2	293.8	279.7	281.9
3	297.3	280.8	279.7	285.9

the central thin-wall area. The results indicate no cracks, or shrinkage in either the central thin-walled area or the end of the casting, ensuring the strength of the key load-bearing parts.

Tensile testing results are shown in Table 4. The tensile strength of the specimens exceeds 800 MPa, elongation is greater than 6%, and the hardness exceeds 270 HV, all meeting the mechanical property requirements for 800-5. This confirms that the optimized process meets the production, processing, and operational standards for the crossbeam castings.

Table 5 presents hardness test results for specimens at positions 1, 2, and 3. The hardness values are consistent across all areas, with an average hardness of 283.97 HV, exceeding the required 270 HV and indicating that the castings are sufficiently solidified under the current technological scheme, with minimal shrinkage.

CONCLUSIONS

Simulations of the 800-5 crossbeam's sand casting, filling, and solidification stages were conducted with various gating system. The optimal casting technique was identified by elevating the number of risers from 4 to 8, adjusting the pouring speed to 10 cm/s, and maintaining a temperature of 1380 °C. Under these conditions, the casting's shrinkage decreased by 9.36%, from 751.16 mm³ to 680.85 mm³.

Metallographic analysis of samples from different crossbeam locations revealed a spheroidization grade of 2, effective spheroidization, and more than 90% pearlite content in the matrix, with optimal microstructure organization. Mechanical testing confirmed that the tensile specimens met the 800-5 standards. Hardness tests showed values above 270 HV, indicating the casting's suitability for production and use.

Acknowledgements

The authors acknowledge the Project commissioned by Hefei Jianghuai Casting LTD. (W2023JSKF0487), Hefei Common Technology Research and Development "Unveiling and Leading" Project (2022-SZD-0029).

REFERENCES

1. Avikal S, Bisht A, Sharma D, et al. Design and fatigue analysis of front axle beam of a heavy duty truck using ansys[J]. Materials Today: Proceedings, 2020; 26. https://doi.org/10.1016/j.matpr.2020.02.901
2. Su, T., He, T., Yang, R., et al. Topology optimization and lightweight design of stamping dies for forming automobile panels. Advanced Manufacturing Technology, 2022; 121: 4691–4702. https://doi.org/10.1007/s00170-022-09683-2
3. Chen, J., Kwak, Y., Xu, M., et al. Topology and modular size optimization of small electric vehicle frame based on cross-section contribution analysis. Structural and Multidisciplinary Optimization, 2021; 64(6): 4287–4304. https://doi.org/10.1007/s00158-021-03075-y
4. Wang, Z., Suiker, A.S.J., Hofmeyer, H., et al. Optimization of thin-walled beam structures: monolithic versus staggered solution schemes. Thin-Walled Structures, 2021; 159. https://doi.org/10.1016/j.tws.2020.107182
5. Weeger, O., Narayanan, B., Dunn, M.L. Isogeometric shape optimization of nonlinear, curved 3d beams and beam structures. Computer Methods in Applied Mechanics and Engineering, 2019, 345:

26–51. https://doi.org/10.1016/j.cma.2018.10.038

6. Akinribide, O.J., Ogundare, O.D., Oluwafemi, O.M., Ebisike, K., Nageri, A.K., Akinwamide, S.O., Gamaoun, F., Olubambi, P.A. A review on heat treatment of cast iron: phase evolution and mechanical characterization. Materials 2022; 15: 7109. https://doi.org/10.3390/ma15207109
7. Liu, R., Wang, C., Liu, Z. Numerical simulation study on sand casting of shaft seat based on ProCAST. Foundry Technology, 2016; 37(1): 87–90. https://doi.org/CNKI: SUN: ZZJS.0.2016-01-037
8. Fan, X., Wang, Z., Long, Z., et al. Optimization of impeller casting process based on ProCAST. China Foundry Equipment and Technology, 2014; 4: 11–13. https://doi.org/10.3969/j.issn.1006-9658.2014.04.003
9. Chaengkham, P., Srichandr, P. Continuously cast ductile iron: processing, structures, and properties. Journal of Materials Processing Technology, 2011; 211(8): 1372–1378. https://doi.org/10.1016/j.jmatprotec.2011.03.008
10. Liu, S., Zhan, J., Huang, Y. Application of casting process simulation technology based on testing and verification of coal machine rocker arm. Thermal Processing Technology, 2017; 46(8): 122–125. https://doi.org/10.14158/j.cnki.1001-3814.2017.15.030
11. Liu J.H., Yan J.S., Zhao X.B., et al. Precipitation and evolution of nodular graphite during solidification process of ductile iron. China Foundry, 2020; 17(4): 260-271. https://doi.org/10.1007/s41230-020-0042-2
12. Deng, Y. Numerical simulation and process optimization of the casting process of large ductile iron parts. PhD thesis, Hunan University, 2013. https://doi.org/10.7666/d.Y2355261
13. Xiang, S., Liu, L., Li, Y., et al. Research on casting process design and ductile iron plate spring seat organization based on numerical simulation[J]. Casting, 2022; 71(05): 625–631.
14. Małysza M., Żuczek R., Wilk-Kołodziejczyk D., et al. Technological optimization of the stirrup casting process with the use of computer simulations. Materials 2022; 15(19). https://doi.org/10.3390/MA15196781